Catalysis by Au@pNIPAM Nanocomposites: Effect of the Cross-Linking Density

Susana Carregal-Romero,[†] Niklaas J. Buurma,[‡] Jorge Pérez-Juste,*,[†] Luis M. Liz-Marzán,[†] and Pablo Hervés*,[†]

[†]*Departamento de Química Física, Universidade de Vigo, E-36310, Vigo, Spain, and* [‡]*Physical Organic Chemistry Centre, School of Chemistry, Cardiff University, Main Building, Park Place, Cardiff, CF10 3AT, United Kingdom*

Gold nanoparticles encapsulated in a thermoresponsive microgel (pNIPAM) were used as catalysts in the electron-transfer reaction between hexacyanoferrate(III) and borohydride ions. The thermosensitive pNIPAM network can act as a "nanogate" that can be opened or closed to a certain extent, thereby controlling the diffusion of reactants toward the catalytic core. Interestingly, the crosslinker density plays an important role, because it defines the thermal response of the Au@pNIPAM system and, in turn, the extent of the volume change and therefore the polymeric density. The catalytic activity of the encapsulated gold nanoparticles is thus affected both by temperature and by the composition of the shell. A mathematical model reproducing the key features of the temperature-controlled catalysis by our thermosensitive nanoparticles confirms the effect of diffusion rate through the shell on the actual reaction rate.

Introduction

Metal nanoparticles and nanocomposites have attracted a great deal of attention, because of their potential applications in several fields, such as catalysis,[1,2] photonics, electronics, optics, biomedicine,[3] and biosensing.[4] In particular, core/shell nanoparticle architectures, in which a layer of inorganic or organic material surrounds a metal nanoparticle core, have been investigated both as a means to improve the stability and surface chemistry of the core nanoparticle and as a way of accessing unique physical properties that are not possible from one nanomaterial alone.[5] For example, the silica coating of metal nanoparticles is interesting because of the numerous applications in many fields of materials and biomaterials science. Ung et al. have shown that metal nanoparticles encapsulated within thin silica shells can catalyze redox reactions on their surface.[6] Lee et al. have shown that silica shells enhance the colloidal stability of nanoparticles, and a precise tuning of the shell porosity allows control over the catalytic activity through variation of the diffusion rate of the reactants through the shell.[7,8] Joo et al. have shown that the coating of platinum nanoparticles with a mesoporous silica shell confers them with a higher stability,[9,10] allowing the particles to be heated up to temperatures approaching 1000 K without evidence of sintering. Although the nanoparticles were buried, the catalytic activity was not inhibited; the silica shell was sufficiently porous to allow transport of catalytic reactants and products to and from the surface of the platinum nanoparticle.[10]

Additional advantages can be obtained if stimuli-responsive polymeric shells are fabricated, because they offer possibilities for external switching and manipulation.[11,12] A common example is poly(*N*-isopropylacrylamide) (pNIPAM), which is a thermoresponsive polymer that undergoes a phase transition from a hydrophilic, water-swollen state to a hydrophobic, globular state when heated above its lower critical solution temperature (LCST), which is ∼32−34 °C, in water.[13] The addition of cross-linkers and co-monomers has also been proposed, as a means to control the swelling/shrinking ratio of the microgels and to add responsiveness toward different stimuli such as temperature,[14] pH,[15,16] ionic

*Author to whom correspondence should be addressed. Fax: +34 986812556. E-mail addresses: juste@uvigo.es (J.P.-J.), jherves@uvigo.es (P.H.).

(1) Lim, B.; Jiang, M.; Camargo, P. H. C.; Cho, E. C.; Tao, J.; Lu, X.; Zhu, Y.; Xia, Y. *Science* **2009**, *324*, 1302–1305.
(2) Schrinner, M.; Ballauff, M.; Talmon, Y.; Kauffmann, Y.; Thun, J.; Möller, M.; Breu, J. *Science* **2009**, *323*, 617–620.
(3) Huang, X.; Jain, P. K.; El-Sayed, I. H.; El-Sayed, M. A. *Nanomedicine* **2007**, *2*, 681–693.
(4) Scodeller, P.; Flexer, V.; Szamocki, R.; Calvo, E. J.; Tognalli, N.; Troiani, H.; Fainstein, A. *J. Am. Chem. Soc.* **2008**, *130*, 12690–12697.
(5) Guerrero-Martínez, A.; Pérez-Juste, J.; Liz-Marzán, L. M. *Adv. Mater.* **2010**, *22*, 1182−1195.
(6) Ung, T.; Liz-Marzán, L. M.; Mulvaney, P. *J. Phys. Chem. B* **1999**, *103*, 6770–6773.

(7) Lee, J.; Park, J. C.; Song, H. *Adv. Mater.* **2008**, *20*, 1523–1528.
(8) Lee, J.; Park, J. C.; Bang, J. U.; Song, H. *Chem. Mater.* **2008**, *20*, 5839–5844.
(9) Gorelikov, I.; Matsuura, N. *Nano Lett.* **2008**, *8*, 369–373.
(10) Joo, S. H.; Park, J. Y.; Tsung, C.-K.; Yamada, Y.; Yang, P.; Somorjai, G. A. *Nat. Mater.* **2009**, *8*, 126–131.
(11) Kang, Y.; Erickson, K. J.; Taton, T. A. *J. Am. Chem. Soc.* **2005**, *127*, 13800–13801.
(12) Suzuki, A.; Tanaka, T. *Nature* **1990**, *346*, 345–347.
(13) Pelton, R. *Adv. Colloid Interface Sci.* **2000**, *85*, 1–33.
(14) Berndt, I.; Popescu, C.; Wortmann, F.-J.; Richtering, W. *Angew. Chem., Int. Ed.* **2006**, *45*, 1081–1085.
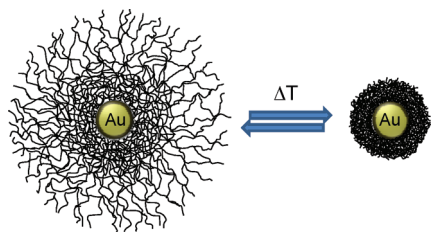
Figure 1. Schematic representation of an Au@pNIPAM composite nanoparticle consisting of a gold core and thermosensitive polymer shell. The pNIPAM shell can reversibly swell or collapse below or above the LCST, respectively, when dispersed in water.

strength,[17,18] or light.[19] In that respect, Ballauf's group has shown that metallic nanoparticles of different nature can be prepared in situ in the presence of polystyrene/poly(*N*-isopropylacrylamide) core−shell particles, in such a way that the particles are embedded within the polymer network, so that no additional surface modification was needed to protect these particles from coagulation. Stabilization is solely achieved by the spherical polyelectrolyte brushes in which the alloy nanoparticles are immobilized. These nanocomposites have been proven efficient catalysts for several redox reactions.[20−22] In addition, the thermoresponsive properties of the polymer shell allowed the catalytic activity to be modulated in a nonmonotonous way, by exploiting the temperature-induced phase transition of the network.[23,24]

Regarding the nature of the catalyst, gold nanoparticles were chosen due to the recent research activity in that field. Gold nanoparticles can act as catalysts in many reactions, such as glucose oxidation,[25] CO oxidation,[26] and alcohol oxidation.[27] Since metal nanoparticles have a pronounced tendency to aggregate during the catalytic reactions, the use of supports or stabilizing agents is required. Therefore, the use of pNIPAM as a protecting agent is extra-advantageous, because it makes the nanoparticle not only stable but also thermoresponsive.[28,29] In

the present work, we studied the catalytic activity of a well-defined core−shell system comprising a gold core and a thermoresponsive pNIPAM shell (see Figure 1). In this system, the accessibility of the metal core for chemical moieties in solution, which is crucial for testing its catalytic activity, is defined by the porosity of the shell. The importance of shell porosity has been demonstrated by the success of in situ seeded-growth of the gold cores, in which the specific experimental conditions can modify the diffusion rate of the reactants through the shell, thereby leading to changes in the resulting nanoparticle morphology.[28,29] A similar strategy was recently used to fabricate multifunctional microgels displaying both optical and magnetic response.[30] Thus, such a well-defined core−shell system can be used to study the effect of the temperature-induced swelling−collapse of the polymeric shell on reactants diffusion.[31] In addition, the effect of the cross-linker density, i.e., the interweaved degree of the pNIPAM shell on the catalytic activity of the gold surface, can be analyzed.

For the present study, we selected as a model the electron transfer reaction between hexacyanoferrate(III) and borohydride ions in water. This reaction has been demonstrated to be efficiently catalyzed on both platinum and gold nanoparticle surfaces, as compared with the catalyst-free process.[32,33] In both cases, we showed that (i) the reaction can be followed up to its completion and (ii) no particle aggregation occurs during the catalytic process.

Results and Discussion

pNIPAM-Coated Gold Nanoparticles. The core−shell Au@pNIPAM particles were synthesized by the two-step procedure recently developed in our group for the encapsulation of CTAB-stabilized metal nanoparticles with pNIPAM.[28] The first step comprises the growth of a thin polystyrene (PS) shell within the CTAB bilayer, which serves to avoid aggregation and to enhance the polymerization of NIPAM directly on the gold particle's surface, in the presence of a cross-linker, *N*,*N'*-methylene bisacrylamide (BIS), during the second step. Three Au@pNIPAM samples were prepared with different cross-linker densities by gradually increasing the percentage of BIS in the mixture prior to polymerization, while keeping the amount of NIPAM monomers constant. The molar contents of BIS in these samples were 7%, 10%, and 15%. Figure 2 shows representative TEM images of the pNIPAM-coated gold nanoparticles with different BIS content, upon the removal of core-free microgels through centrifugation (see the Experimental Section). It can be

(15) Das, M.; Mardyani, S.; Chan, W. C. W.; Kumacheva, E. *Adv. Mater.* **2006**, *18*, 80–83.
(16) Karg, M.; Lu, Y.; Carbó-Argibay, E.; Pastoriza-Santos, I.; Pérez-Juste, J.; Liz-Marzán, L. M.; Hellweg, T. *Langmuir* **2009**, *25*, 3163–3167.
(17) Daly, E.; Saunders, B. R. *Phys. Chem. Chem. Phys.* **2000**, *2*, 3187–3193.
(18) López-Leon, T.; Ortega-Vinuesa, J. L.; Bastos-González, D.; Elaiessari, A. *J. Phys. Chem. B* **2006**, *110*, 4629–4636.
(19) Gorelikov, I.; Field, L. M.; Kumacheva, E. *J. Am. Chem. Soc.* **2004**, *126*, 15938–15939.
(20) Schrinner, M.; Proch, S.; Mei, Y.; Kempe, R.; Miyajima, N.; Ballauff, M. *Adv. Mater.* **2008**, *20*, 1928–1933.
(21) Lu, Y.; Mei, Y.; Schrinner, M.; Ballauff, M.; Möller, M. W.; Breu, J. *J. Phys. Chem. C* **2007**, *111*, 7676–7681.
(22) Je, J.; Huynh, T.; Hu, Y.; Yin, Y. *Nano Lett.* **2008**, *8*, 931–934.
(23) Lu, Y.; Mei, Y.; Drechsler, M.; Ballauff, M. *Angew. Chem., Int. Ed.* **2006**, *45*, 813–816.
(24) Lu, Y.; Mei, Y.; Drechsler, M.; Ballauff, M. *J. Phys. Chem. B* **2006**, *110*, 3930–3937.
(25) Thielecke, N.; Aytemir, M.; Pruesse, U. *Catal. Today* **2007**, *121*, 115–120.
(26) Haruta, M. *Chem. Rec.* **2003**, *3*, 75–87.
(27) Han, J.; Liu, Y.; Guo, R. *Adv. Funct. Mater.* **2009**, *19*, 1112–1117.
(28) Contreras-Cáceres, R.; Sánchez-Iglesias, A.; Karg, M.; Pastoriza-Santos, I.; Pérez-Juste, J.; Pacifico, J.; Hellweg, T.; Fernández-Barbero, A.; Liz-Marzán, L. M. *Adv. Mater.* **2008**, *20*, 1666–1670.
(29) Contreras-Cáceres, R.; Pacifico, J.; Pastoriza-Santos, I.; Pérez-Juste, J.; Fernández-Barbero, A.; Liz-Marzán, L. M. *Adv. Funct. Mater.* **2009**, *19*, 3070–3076.

(30) Sánchez-Iglesias, A.; Grzelczak, M.; Rodríguez-González, B.; Guardia-Girós, P.; Pastoriza-Santos, I.; Pérez-Juste, J.; Prato, M.; Liz-Marzán, L. M. *ACS Nano* **2009**, *3*, 3184–3190.
(31) Alvarez-Puebla, R.; Contreras-Cáceres, R.; Pastoriza-Santos, I.; Pérez-Juste, J.; Liz-Marzán, L. M. *Angew. Chem., Int. Ed.* **2009**, *48*, 138–143.
(32) Pastoriza-Santos, I.; Pérez-Juste, J.; Carregal-Romero, S.; Hervés, P.; Liz-Marzán, L. M. *Chem.−Asian J.* **2006**, *1*, 730–736.
(33) Sanles-Sobrido, M.; Correa-Duarte, M. A.; Carregal-Romero, S.; Rodríguez-González, B.; Álvarez-Puebla, R. A.; Hervés, P.; Liz-Marzán, L. M. *Chem. Mater.* **2009**, *21*, 1531–1535.
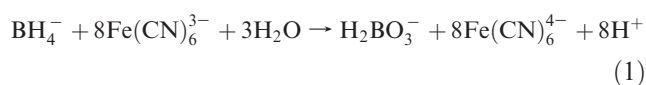
Article

Chem. Mater., Vol. 22, No. 10, 2010 3053
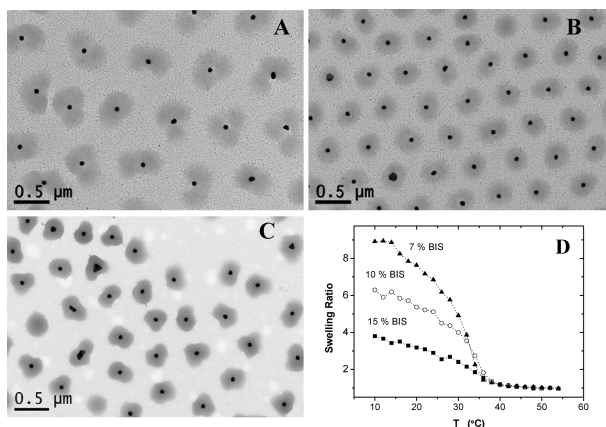
Figure 2. (A−C) TEM images of Au@pNIPAM particles containing 7% (panel A), 10% (panel B), and 15% (panel C) *N,N'*-methylene bisacrylamide. (D) Variation of the swelling ratio (α) of the different samples (as indicated) with temperature (see text for details).

Table 1. Dimensions of the Different Au@pNIPAM Nanocomposites, as Determined by PCS and TEM

%NIPAM[a]	% BIS[b]	D_H (nm)		α_{max}[c]	d (nm)[d]
		at 10 °C	at 52 °C		
100	15	508.4	325.7	3.8	58.2 ± 4.6
100	10	436.3	236.3	6.3	58.6 ± 4.2
100	7	614.1	296.2	9.1	64.1 ± 4.6

[a] Defined as the standard amount; 0.1698 g NIPAM, see Experimental Section for details. [b] Molar percentage of *N,N'*-methylenebisacrylamide, with respect to NIPAM. [c] Maximum swelling ratio: $\alpha_{max} = V(10 °C)/V(52 °C)$. [d] Average diameter of the gold cores determined by TEM.

clearly seen that all particles are coated and there is no sign of aggregation. At first sight, a higher cross-linking density seems to lead to thinner microgel shells, which can be related to the ability of the microgel shell to spread on the TEM grid during the drying process.[29]

The thermoresponsive properties of these core−shell systems were initially characterized by photon correlation spectroscopy (PCS). The swelling behavior, defined as the ratio between the volume of the particle at a given temperature and that of the particle in the fully collapsed state ($\alpha = V(T)/V_{collapsed}(52 °C)$), is shown in Figure 2D for these particular samples. In all cases, a well-defined volume phase transition temperature was determined at ∼32−34 °C, with a slope that increased for lower cross-linker contents, as previously reported.[29] Figure 2D also demonstrates that the relative swelling of the microgel decreases as the cross-linking density increases. In particular, a decrease in the BIS content (from 15% down to 7%) produces an increase in the fully swollen volume of ∼2.4-fold (see Table 1).

Catalysis with Au@pNIPAM. We studied the catalytic activity of the nanocomposites, with regard to the reduction of hexacyanoferrate(III) by borohydride ions in aqueous solution, which has been proposed as a model reaction to evaluate the catalytic activity of gold nanoparticles.[34] The redox reaction can be written as[35]

$$BH_4^- + 8Fe(CN)_6^{3-} + 3H_2O \rightarrow H_2BO_3^- + 8Fe(CN)_6^{4-} + 8H^+ \tag{1}$$

In the presence of gold nanoparticles, the reaction proceeds through a two-step process. In the first step, borohydride injects electrons on the particles, which act as a reservoir and become cathodically polarized, whereas in the second and slow step, ferricyanide ions diffuse toward the nanoparticle surface and are reduced by excess surface electrons. Also note that the

noncatalyzed reaction pathway (eq 1) can be neglected, because it is very slow, compared to the catalyzed reaction.[34] In addition, it is worth mentioning that, in all experiments, we worked at basic pH, to minimize the decomposition of borohydride,[36] and at a borohydride concentration in large excess with respect to hexacyanoferrate(III) ions. Thus, the kinetics of the reduction process can be treated as a pseudo-*n*th-order reaction, following the equation

$$-\frac{d[Fe(CN)_6^{3-}]}{dt} = k_{obs}[Fe(CN)_6^{3-}]^n \tag{2}$$

The progress of the reduction was monitored through changes in the ultraviolet−visible (UV−vis) spectrum of hexacyanoferrate(III) (see Figure 3A). The characteristic hexacyanoferrate(III) absorption band at 420 nm was observed to decrease with time as reduction into ferrocyanide proceeded, offering a good correlation with first-order kinetics, as shown in Figure 3B.

From the spectra shown in Figure 3A, it can be clearly observed that, during the period required for complete disappearance of the hexacyanoferrate(III) absorption band, the surface plasmon band (535 nm) of the gold nanoparticles remained totally unchanged, which is a clear evidence that the colloid is stable. Figure 3B shows a typical kinetic trace highlighting the high-quality, first-order nature of the reaction.

To check the reproducibility/reusability of Au@pNIPAM as a catalyst, the reduction of hexacyanoferrate-(III) was repeated several times, using the same colloidal solution, through sequential addition of $K_3Fe(CN)_6$ to an aqueous solution containing excess borohydride and a constant concentration of Au@pNIPAM nanoparticles. Figure 4 shows the kinetic trace at 420 nm and the calculated rate constant for each addition. It is obvious from this plot that the first-order kinetic behavior was perfectly reproducible, as predicted by eq 2. Although the reaction half-life time increased from 8.1 s to 9.3 s between the first and fourth additions of hexacyanoferrate(III), note that after each addition, the final volume increased by 0.8%, leading to a slight decrease in borohydride and gold nanoparticle concentration. This experiment is a clear evidence for the stability of

(34) Carregal-Romero, S.; Pérez-Juste, J.; Mulvaney, P.; Hervés, P.; Liz-Marzán, L. M. *Langmuir* **2010**, *26*, 1271–1277.
(35) Freund, T. J. *Inorg. Nucl. Chem.* **1959**, *9*, 246–251.
(36) Bhattacharjee, M.; Bhattacharjee, A. K.; Mahanti, M. K. *Bull. Chem. Soc. Jpn.* **1981**, *54*, 3566–3569.
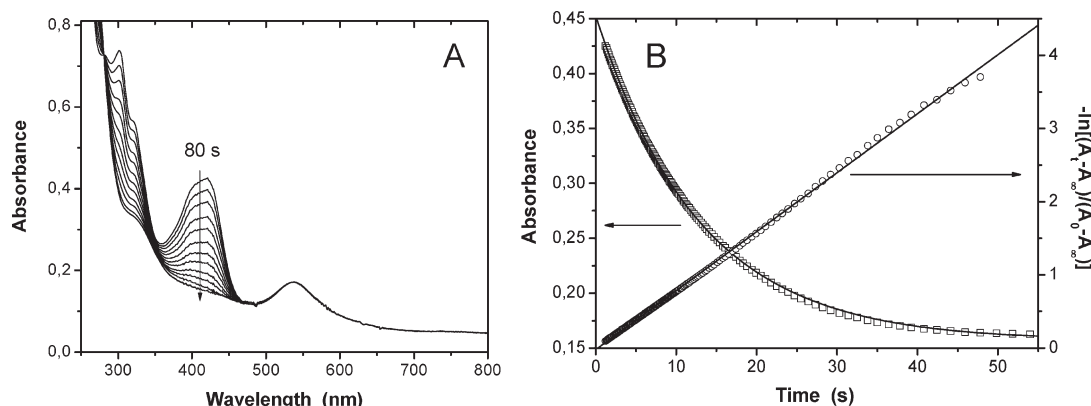
Figure 3. (A) Spectral evolution of a mixture of hexacyanoferrate and Au@pNIPAM nanocomposites upon borohydride addition. $[Fe(CN)_6^{3-}] = 4 \times 10^{-4}$ M, $[BH_4^-] = 0.05$ M, $[Au@pNIPAM]_{NP} = 1.34 \times 10^{-12}$ M. $T = 22$ °C, pH = 12, $t_{1/2} = 8.6$ s. Seven percent (7%) BIS Au@pNIPAM sample. B) Kinetic trace of the absorbance at 420 nm during the reduction of $Fe(CN)_6^{3-}$, and linearized data for first-order analysis corresponding to Figure 3a. $k_{obs} = 0.08$ s^{-1}.
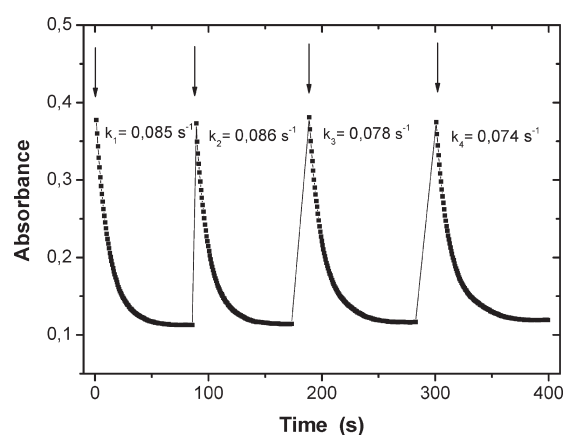


Figure 4. Absorbance kinetic traces at 420 nm, registered during the sequential reduction of $Fe(CN)_6^{3-}$. Initial concentrations: $[Fe(CN)_6^{3-}] = 4 \times 10^{-4}$ M, $[BH_4^-] = 0.05$ M, $[Au]_{NP} = 1.34 \times 10^{-12}$ M. $T = 19$ °C, pH = 12. The arrows indicate the times at which $Fe(CN)_6^{3-}$ was added to obtain $[Fe(CN)_6^{3-}] = 4 \times 10^{-4}$ M.

the Au@pNIPAM composite colloid in the reaction medium, as well as for the reproducibility of its catalytic activity.

Influence of Au@pNIPAM Concentration. The effect of catalyst (gold) concentration on the reaction rate was studied for three Au@pNIPAM colloids with different cross-linking content (7%, 10%, and 15% BIS). Figure 5 shows the influence of Au@pNIPAM concentration for the different cross-linking densities at $T = 15$ °C. In all cases, a linear relationship was obtained between the observed rate constant and the concentration of gold cores. It can also be observed that, for the colloids coated with a shell of lower cross-linking density, the catalytic activity was consistently higher, for the same Au@pNIPAM concentration.

The catalytic effect of the nanoparticles depends on both the concentration and the gold surface area per particle. To highlight this effect, the total surface area per unit solution volume is also indicated in Figure 5 (upper *x*-axis). The linear dependence of the observed rate constant with the total surface area of the metal nanoparticles allows us to rewrite the first-order rate equation
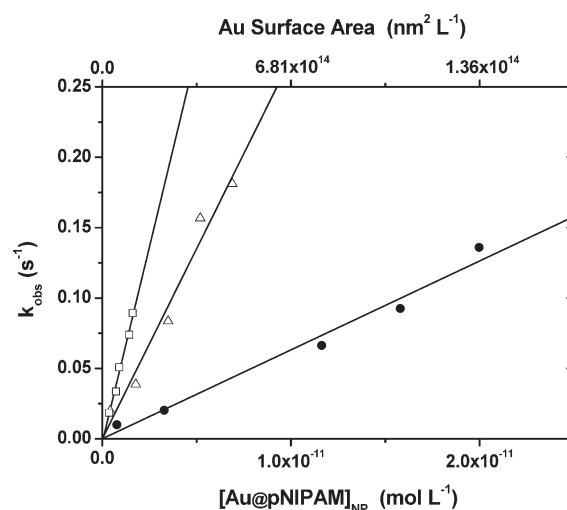

Figure 5. Influence of Au@pNIPAM nanocomposite concentration (lower *x*-axis) and the corresponding gold surface area per unit solution volume (upper *x*-axis) on the observed pseudo-first-order rate constant, for different shell cross-linking densities: (□) 7% BIS, (△) 10% BIS, and (●) 15% BIS. $T = 15$ °C. $[Fe(CN)_6^{3-}] = 4 \times 10^{-4}$ M, $[BH_4^-] = 0.05$ M, pH = 12.

(eq 2) as follows:

$$-\frac{d[Fe(CN)_6^{3-}]}{dt} = k_{obs}[Fe(CN)_6^{3-}]$$

$$= k_S[Au]_{core}A[Fe(CN)_6^{3-}]$$

$$= k_s S[Fe(CN)_6^{3-}] \qquad (3)$$

where A is the gold surface area per particle and k_S the rate constant normalized to the total surface area of gold per unit volume of solution (values of 30.0 nm and 19.2 g/cm^3 for the gold nanoparticle radius and gold density, respectively, were used), and S the total surface area per unit solution volume. Equation 3 accurately predicts the linear trend shown in Figure 5, indicating that the observed rate constant increases with the available gold surface area per unit volume, thus confirming that the catalytic reduction occurs on the surface of the metallic nanoparticles and the catalytic activity therefore depends
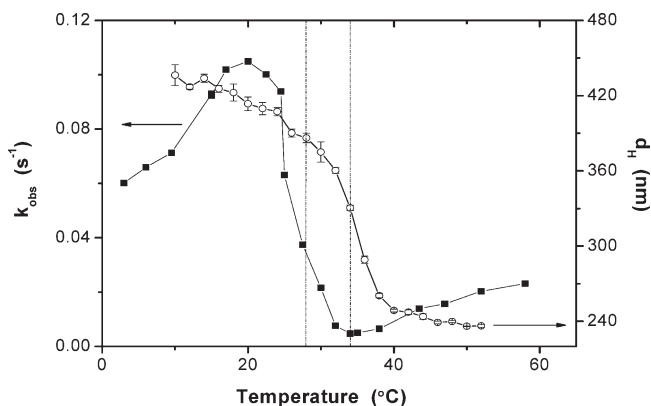
Figure 6. Influence of temperature on the observed pseudo-first-order rate constant, k_{obs}, measured in the presence of 10% BIS Au@pNIPAM, compared with the corresponding hydrodynamic diameters. $[Fe(CN)_6{}^{3-}] = 4 \times 10^{-4}$ M, $[BH_4{}^-] = 0.05$M, $[Au@pNIPAM]_{NP} = 3.41 \times 10^{-12}$ M, pH = 12. The lines indicate the approximate LCST, as determined by PCS and kinetic analysis.

on the total surface area of the gold nanoparticles. Besides, the effect of cross-linking density on the catalytic activity shows us that the diffusion of the reactants through the pNIPAM shell plays an important role in our system. The linear trend can be observed, regardless of the selected temperature, but the reaction rates are obviously influenced by temperature. As an example, Figure S1 in the Supporting Information shows the influence of particle concentration for the case of 15% BIS, at 15 and 44 °C, corresponding to the fully swollen and collapsed states of the microgel, respectively. Counterintuitively, we found that the slope measured at 15 °C was ca. 17.6 times larger than that at 44 °C; this means that an increase in temperature leads to a decrease in the catalytic activity. This behavior can tentatively be ascribed to the change in pNIPAM shell density (porosity) on the diffusion of the reactants, which is discussed in the following section.

Influence of Temperature. Considering the anomalous behavior observed at temperatures around the LCST of the pNIPAM shell (see Figure S1 in the Supporting Information), we decided to perform a more detailed analysis of the influence of temperature on the reduction kinetics. Figure 6 shows the effect of temperature for a Au@pNIPAM colloid where the shells have a BIS content of 10%, while keeping all other reaction conditions constant. Three different regions can clearly be distinguished in this plot: at temperatures of < 20 °C, the observed rate constant increases with temperature, whereas in the region of 20−35 °C, k_{obs} decreases with increasing temperature, and, finally, at > 35 °C, the observed rate constant increases again with temperature. Similar behavior was registered for the two other samples with different BIS contents (see Figure S2 in the Supporting Information).

As indicated above, the explanation of the observed experimental behavior will be based on the thermoresponsive behavior of the pNIPAM shell. Figure 6 (right *y*-axis) shows the variation of the hydrodynamic diameter of the Au@pNIPAM particles with temperature, as

determined by PCS. At low temperature, the pNIPAM shell is in the fully swollen state, because of its high solubility in water; the reactants can easily diffuse through the pores and reach the gold nanoparticle surface, so that the observed rate constant increases with temperature, as expected from Arrhenius' law.[34] In the vicinity of the LCST (32−34 °C), the particle diameter starts to decrease (the shell shrinks), because of the lower solubility of pNIPAM in water, which leads to the expulsion of water and compression of the porous network. This decrease in porosity affects the diffusion of reactants through the polymer shell, which slows down as the temperature is increased, thus leading to a decrease in the observed rate constant. The results indicate that this decrease in the diffusion coefficients is not compensated by the Arrhenius-like increase of reaction rate with temperature (vide infra). Once the shell is fully collapsed, the diffusion of reactants is no longer affected by changes in the polymer shell and further temperature increases again lead to a gradual increase in the observed rate constant.

It should be indicated that the LCST values determined from light scattering and from the kinetic data are slightly different. Although analysis of the PCS data provides a LCST value similar to that reported for pure pNIPAM (32−34 °C),[13,28] the kinetic data show a shift in the phase-transition temperature toward lower temperatures (27−28 °C). Although not expected, this difference can be explained considering many facts that have been reported for pNIPAM polymerization and properties (see, for instance, ref 37). It has been reported that, as a result of the different hydrophobicity and polymerization rates of NIPAM and bisacrylamide, their distribution within the microgel is far from homogeneous.[37] A core−shell model was thus proposed for pure pNIPAM microgels, where the core would contain the majority of cross-linker molecules.[13,37] The overall swelling behavior of the particle is dominated by the swelling of the outer, less-cross-linked regions of the microgel, at temperatures near the LCST.[38] Some studies of the deswelling process using fluorescence nonradiative energy transfer (NRET) concluded that deswelling starts in the external part of the pNIPAM spheres at lower temperatures than those in the core.[39] The consequence is that the transition behavior depends on a subtle balance between the ability by the amide groups of the NIPAM and BIS units to form hydrogen bonds with water, and the hydrophobic interaction of the monomer units with each other. Because the BIS unit is more hydrophilic than NIPAM at elevated temperature,[40] and BIS density is higher near the particle surface, the external part is more hydrophobic and collapses at lower temperature. This can explain the lower LCST obtained from the kinetic data. Because the microgel

(37) Hoare, T.; Pelton, R. *Curr. Opin. Colloid Interface Sci.* **2008**, *13*, 413–428.
(38) Stieger, M.; Richtering, W.; Pedersen, J. S.; Lindner, P. *J. Chem. Phys.* **2004**, *120*, 6197–6206.
(39) Gan, D.; Lyon, L. A. *Anal. Chim. Acta* **2003**, *496*, 53–63.
(40) Matsumura, Y.; Iwai, K. *J. Colloid Interface Sci.* **2006**, *296*, 102–109.
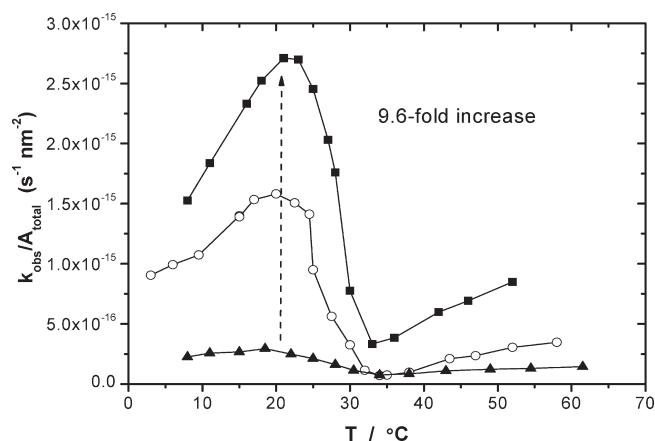
Figure 7. Influence of the cross-linking density on the catalytic activity of gold nanoparticles. $[Fe(CN)_6^{3-}] = 4 \times 10^{-4}$ M, $[BH_4^-] = 0.05$M, pH = 12. Gold surfaces: (■) 2.61×10^{13} nm^2 for 7% BIS, (○) 6.64×10^{13} nm^2 for 10% BIS, and (▲) 6.64×10^{13} nm^2 for 15% BIS.

shell can slow down the diffusion of reactants at lower temperatures, we suggest that the internal inhomogeneities present in the pNIPAM shell are registered at lower temperature in the kinetic data (slowing down the diffusion of the reactants) than in PCS, which shows an overall change in particle size without taking into account the internal structure of the shell.

Influence of Cross-Linking Density. Finally, we analyze the influence of the microgel cross-linking density on the profile of the catalytic activity versus temperature. Figure 7 shows the observed rate constants, normalized by the total gold surface area, for three samples with different BIS content. As noted in the previous section, a similar trend was observed for all three cases: increasing rate constants at temperatures of < 20 °C, followed by a decrease in rate constants in the range of 20−35 °C (microgel shell collapse), and finally increasing rate constants at > 35 °C. As general observations, we can say that the normalized rate constant is higher when the shell has a lower cross-linker content, and that the slopes are consistently larger as the percentage of BIS decreases. This overall trend can be understood as an effect of the cross-linking density of pNIPAM, which leads to a decrease in microgel porosity at denser cross-linking.[41] Theoretically estimated pore size values of 2.4 and 4.1 nm have been reported for microgels with cross-linker densities of 7.4 and 4.4 mol %, respectively.[41] Since the cross-linking distribution is radial, it is also expected that the pore size increases from the center of the particle toward the periphery.[42] This effect can be exemplified at 20 °C, where the normalized k_{obs} reaches a maximum in all cases, but decreasing the cross-linking density by a factor 2.1 (from 15% to 7% BIS) leads to a 9.6-fold increase in the value of k_{obs}/A_{total}. However, in the fully collapsed state, at 34 °C, the value of k_{obs}/A_{total} reaches a minimum, which is similar for the samples with 10% and 15% BIS but is higher by a factor of 4 for 7% BIS. These differences between the swollen and collapsed states

could be explained by simply considering a different cross-linking degree of the pNIPAM chains, leading to a higher or lower porosity, making diffusion of the reactants through the polymeric shell easier or more difficult, respectively. Similar results were previously reported by Lu et al. for thermosensitive core−shell particles consisting of a polystyrene core and a pNIPAM shell with different cross-linking degrees and doped with silver nanoparticles. However, despite the relatively similar swelling ratios, the small thickness of the pNIPAM shell leads to a much-less-pronounced cross-linking effect in their case.[24]

Kinetic Modeling. In all cases, the kinetic traces follow pseudo-first-order kinetics, indicating that a steady-state situation is reached very rapidly. If a steady-state situation had not been reached rapidly, the kinetics would have shown an induction period.[43] Within each temperature regime (that is, below and above the LCST), we consider the pNIPAM shell as a hollow shell (or spherical wall) of constant properties with inner diameter r_i and outer diameter r_o. A reaction occurring at the surface of the nanoparticle then involves diffusion of a reactant R across the nanoparticle shell with a diffusion coefficient $D_{R,s}$, followed by reaction at the surface of the nanoparticle with a rate constant k_{surf}. We assume a homogeneous distribution of the reactant outside the nanoparticle shell, i.e., conditions of perfect mixing or at least fast diffusion of the reactant in the bulk solvent compared to diffusion in the nanoparticle shell. Under such conditions, the reactant concentration in bulk solvent is identical to the concentration at the outer limit of the nanoparticle shell, $[R]_o$. The reactant concentration at the inner limit of the shell, i.e., at the surface of the nanoparticle core, is given as $[R]_i$. Figure S1 in the Supporting Information summarizes the complete process. Under steady-state conditions, within each temperature regime, and assuming that the fractional amount of reactant at the inside of the shell and within the shell is small compared to the total concentration of reactant (i.e., $[R]_o \sim [R]_{total}$), the overall temperature dependence of k_{obs} results from the combined temperature dependence of k_{surf} and $D_{R,s}$, for which Arrhenius-type behavior is found in most liquids[44] (eq 4). (For the full derivation of eq 4, see the Supporting Information.)

$$k_{obs}(T) = k_{surf}(T)\left[\frac{4\pi(\frac{r_i r_o}{r_o - r_i})N_A D_{R,s}(T)}{k_{surf}(T) + 4\pi(\frac{r_i r_o}{r_o - r_i})N_A D_{R,s}(T)}\right]$$

(4)

In the case of a temperature-sensitive permeable shell, such as pNIPAM, the extended-collapsed transition can be approximated as a two-state transition with a temperature-dependent equilibrium constant $K_{collapse}$ (see

(41) Bradley, M.; Vincent, B. *Langmuir* **2005**, *21*, 8630–8634.
(42) Saunders, B.; Vincent, B. *Adv. Colloid Interface Sci.* **1999**, *80*, 1–25.

(43) Crank, J. *The Mathematics of Diffusion*, 2nd Ed.; Oxford University Press: Oxford, U.K., 1975.
(44) North, A. M. *The Collision Theory of Chemical Reactions in Liquids*; Methuen & Co Ltd: London, 1964.
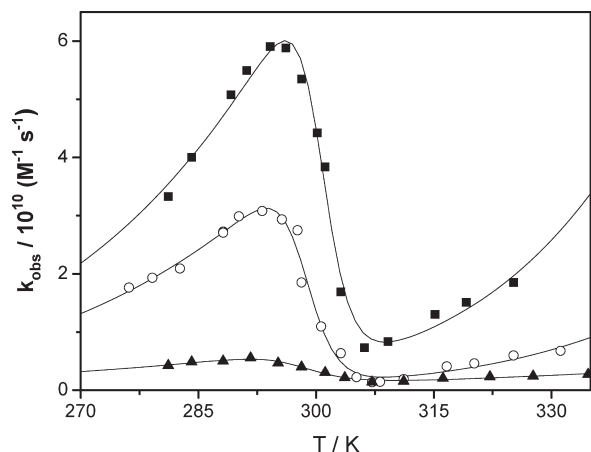
Figure 8. Influence of the temperature on the pseudo-first-order rate constant per gold nanoparticle concentration for the different BIS contents: (■) 7%, (○) 10%, and (▲) 15%. The curves are the result of fitting eq 5 to the experimental data as described in the text.

Figure S3 in the Supporting Information). We distinguish between rate constants below and above the LCST, viz. $k_{\mathrm{obs},T<\mathrm{LCST}}(T)$ and $k_{\mathrm{obs},T>\mathrm{LCST}}(T)$, resulting in eq 5 for the overall temperature dependence of the observed rate constant:

$$k_{\mathrm{obs, global}} = \left(\frac{1}{1+K_{\mathrm{collapse}}(T)}\right) k_{\mathrm{obs},\,T<\mathrm{LCST}}(T)$$
$$+ \left(\frac{K_{\mathrm{collapse}}(T)}{1+K_{\mathrm{collapse}}(T)}\right) k_{\mathrm{obs},\,T>\mathrm{LCST}}(T) \qquad (5)$$

Figure 8 shows the best fit of eq 5 to the kinetic data for the three nanocomposites, and Table S1 in the Supporting Information summarizes the resulting parameters obtained.[45] The obtained parameters show that increasing fractions of cross-linker result in decreasing enthalpy changes for the shell collapse. This decrease in $\Delta H_{\mathrm{collapse}}$ corresponds to a reduced cooperativity of the transition and is typically attributed to shorter interacting stretches of pNIPAM driving the collapse of the gel. This, in turn, results in broader transitions for more extensively cross-linked gels.[46] Long stretches of pNIPAM with just sufficient cross-linking to make the interaction intramolecular, on the other hand, result in strongly cooperative (i.e. steep) transitions.

The parameters in Table S1 in the Supporting Information allow us to calculate the midpoint of the pNIPAM transition T_{collapse} for the pNIPAM shell (see Table 2). The kinetic parameters are further analyzed in terms of the limiting models, i.e. either assuming the reaction at the nanoparticle surface to be fully rate-determining or assuming that diffusion is fully rate-determining. Surface rate constants and diffusion coefficients for both assumptions are summarized in Table 2.

The kinetic parameters in Table 2 show that the phase-transition temperature for the pNIPAM shell is virtually constant for all percentages of cross-linker used, as expected for a cross-linked gel. If we assume k_{surf} to be fully rate-determining, then the calculated rate constants for the surface reaction are very similar to values typically expected for diffusion-controlled reaction. Analogously, if we assume diffusion to be fully rate-determining, the calculated diffusion coefficients for reactant diffusion through the fully extended pNIPAM shell are only slightly lower than the self-diffusion coefficient of water $(23 \times 10^{-8}\ \mathrm{dm^2\ s^{-1}}$ at 298.2 K)[47] and are similar to the value of $9.0 \times 10^{-8}\ \mathrm{dm^2\ s^{-1}}$ for $Fe(CN)_6^{3-}$ in dilute aqueous solution at 298.2 K.[48] The observation that the Arrhenius activation energy increases when going above the LCST (Table S1 in the Supporting Information) is also consistent with a model where diffusion is rate-limiting; the collapsed pNIPAM gel can be envisaged to require more energy for the reactant to move. Despite the indications that the diffusion is rate-limiting, effects on k_{surf} cannot be excluded completely, because it is easily conceivable that k_{surf} is subject to changing medium effects upon pNIPAM shell collapse.

It is also interesting to evaluate the factors required for efficient temperature control of catalysis for nanoparticles encapsulated within a thermoresponsive shell. The interpretation of the activation parameters is difficult because k_{obs} incorporates both diffusion through the pNIPAM shell and the reaction at the nanoparticle surface, and is further complicated by parameter correlation (see the Supporting Information). Nevertheless, it is possible to analyze the properties and dimensions of the nanoparticle shell required for the observed temperature control of nanoparticle catalysis. Here, we assume fully rate-determining diffusion, but analogous arguments are valid for partially rate-determining diffusion. The key factor controlling the effect of nanoparticle shell collapse in eq 4 is given by the term shown in expression 6:

$$\left(\frac{r_{\mathrm{i}} r_{\mathrm{o}}}{r_{\mathrm{o}} - r_{\mathrm{i}}}\right) D_{\mathrm{R,s}} \qquad (6)$$

Upon shell collapse, the term $r_{\mathrm{i}} r_{\mathrm{o}}/(r_{\mathrm{o}} - r_{\mathrm{i}})$ will increase but the diffusion coefficient $D_{\mathrm{R,s}}$ will decrease. The product in eq 6 must decrease for nanoparticle catalysis to be retarded upon shell collapse. For the current design involving an extensive pNIPAM shell around a relatively small catalytic nanoparticle, the increase in the term $r_{\mathrm{i}} r_{\mathrm{o}}/(r_{\mathrm{o}} - r_{\mathrm{i}})$ is minimal (see Table 2). On the other hand, the decrease in the diffusion coefficient is significant, particularly for the systems involving 7% and 10% cross-linker. This combination results in efficient control of the catalytic activity. An additional advantage of the use of less cross-linker stems from the increased cooperativity of the pNIPAM transition (vide supra), allowing

(45) The fitting procedure was performed with *Mathematica*; see the Supporting Information for details.
(46) Woodward, N. C.; Chowdhry, B. Z.; Snowden, M. J.; Leharne, S. A.; Griffiths, P. C.; Winnington, A. L. *Langmuir* **2003**, *19*, 3202–3211.
(47) Krynicki, K.; Green, C. D.; Sawyer, D. W. *Faraday Discuss.* **1978**, *66*, 199–208.
(48) *CRC Handbook of Chemistry and Physics*, 74th Ed.; CRC Press: London, 1993−1994.

Table 2. Kinetic Parameters Obtained through the Fitting of eq 5 to the experimental data. See SI for Further Details about the Fitting Procedure

	7%	10%	15%
T_{collapse}	301 K	298 K	298 K
Assuming Rate-Determining Reaction at the NP Surface			
k_{surf}			
at 290 K	5.1×10^{10} M^{-1} s^{-1}	2.9×10^{10} M^{-1} s^{-1}	0.6×10^{10} M^{-1} s^{-1}
at 310 K	0.8×10^{10} M^{-1} s^{-1}	0.2×10^{10} M^{-1} s^{-1}	0.2×10^{10} M^{-1} s^{-1}
Assuming Rate-Determining Diffusion to the NP Surface			
$r_{\text{i}}r_{\text{o}}/(r_{\text{o}} - r_{\text{i}})$			
at 10 °C	36 nm	33 nm	33 nm
at 52 °C	40 nm	38 nm	35 nm
$D_{\text{R,s}}$			
at 290 K	18.6×10^{-8} dm^2 s^{-1}	11.7×10^{-8} dm^2 s^{-1}	2.2×10^{-8} dm^2 s^{-1}
at 310 K	2.6×10^{-8} dm^2 s^{-1}	0.8×10^{-8} dm^2 s^{-1}	0.6×10^{-8} dm^2 s^{-1}

catalysis to be controlled over narrow temperature ranges. Finally, for efficient control over catalytic efficiency of nanoparticles by a thermosensitive shell, the rate of the reaction must be controlled by diffusion through the nanoparticle shell to a significant extent. If this is not the case, k_{surf} becomes the dominant term in k_{obs} (vide supra) and k_{surf} will be sensitive to medium effects at best.

Conclusions

In summary, we have demonstrated that pNIPAM-gold nanoparticles act as an efficient, thermoresponsive catalyst for the reduction of ferricyanide ions by borohydride in aqueous solution. The catalytic activity can be tuned in a peculiar manner, through changes in the temperature of the solution. The diffusion of the reactants through the shell—and, therefore, the catalysis—are affected by both the cross-linking density and temperature, affecting the catalytic efficiency of the nanocomposite colloids. A kinetic model for the observed rate constant for systems combining diffusion through a nanoparticle shell with reaction at the surface of the nanoparticle was derived using the steady-state approximation. This kinetic model was combined with a two-state thermodynamic model describing pNIPAM shell collapse, resulting in an equation describing the overall temperature dependence of the kinetics for catalysis by nanoparticles encapsulated within a thermosensitive shell. These equations allow the analysis of the factors required for efficient temperature control of Au@pNIPAM nanocomposites. Systems involving an extensive thermoresponsive shell with limited cross-linking, such as the system presented here, allow for particularly efficient control of the catalysis.

Experimental Section

Materials. Ascorbic acid (AA), cetyltrimethylammonium bromide (CTAB), styrene, divinylbenzene and *N*-isopropylacrylamide (NIPAM, 97%), sodium borohydride, and sodium hydroxide were supplied by Aldrich. HAuCl$_4$·3H$_2$O and trisodium citrate dihydrate were supplied by Sigma. *N*,*N'*-methylenebisacrylamide (BIS) was supplied by Fluka. 2,2'-azobis(2-methylpropionamidine) dihydrochloride was supplied by Acros Organics. Potassium hexacyanoferrate(III) was purchased from Scharlab. All reactants were used without further purification.

Water was purified using a Milli-Q system (Millipore, Bedford, MA).

Synthesis of Au@pNIPAM Composites. pNIPAM-coated gold nanoparticles were prepared through a simple two-step method developed by Contreras-Cáceres et al.[28,29] In a typical synthesis, gold nanoparticles with a diameter of 59 ± 4 nm were prepared through a seeded growth method,[49] based on the reduction of HAuCl$_4$ with ascorbic acid on CTAB-stabilized gold nanoparticle seeds (~15 nm, prepared by citrate reduction), in the presence of 0.015 M CTAB. Subsequently, the particles were coated with polystyrene as follows: 150 mL of as-prepared CTAB-stabilized gold nanoparticles were centrifuged at 4500 rpm for 40 min, the supernatant was discarded, and the precipitate redispersed in 150 mL of Milli-Q water. The solution was then heated to 30 °C, followed by the addition of styrene (10 μL) and divinylbenzene (5 μL) under stirring. After 15 min, the temperature was increased to 70 °C and the polymerization was initiated by adding 2,2'-azobis(2- methylpropionamidine) dihydrochloride (20 μL 0.1 M in water). The polymerization was allowed to proceed for 2 h. The solution was centrifuged at 4000 rpm (40 min), the supernatant was discarded, and the precipitate was redispersed in 15 mL of Milli-Q water. The solution was purged with nitrogen (15 min), followed by addition of *N*-isopropylacrylamide (0.1698 g, 1.503 mmol, 100%, referred to as the standard amount) and *N*,*N*-methylenebisacrylamide (0.0234 g, 0.150 mmol, 10% content with respect to NIPAM). After 15 min, the nitrogen flow was stopped and the polymerization was initiated with the addition of 2,2'-azobis(2-methylpropionamidine) dihydrochloride (90 μL 0.1M). After 7−10 min, the reddish solution became turbid and the reaction was allowed to proceed for 3 h at 70 °C. The white mixture was then allowed to cool down to room temperature under stirring. To remove small oligomers and unreacted monomers, as well as gold free microgels, the dispersion was diluted with water (15 mL) and centrifuged (30 min at 4000 rpm) and redispersed in water three times. The cross-linking density was varied by keeping the amount of NIPAM constant (0.1698 g, 1.503 mmol, 100%) and varying the amount of *N*,*N'*-methylenebisacrylamide (16.4 mg, 0.106 mmol, 7%; 23.4 mg, 0.151 mmol, 10%; and 35.1 mg, 0.226 mmol, 15%).

ICP-AES Analysis. Two milliliters (2 mL) of each sample (Au@pNIPAM with 7%, 10%, and 15% BIS) were mixed with 2 mL of aqua regia and progressively digested (15 min at 60, 120, and finally 160 °C). Thereafter, dilution to 25 mL was performed with a primary standard (Nd, 1 mL of aqueous solution, 100 mg/L) before proceeding with the inductively coupled plasma-optical

(49) Rodríguez-Fernández, J.; Pérez-Juste, J.; García de Abajo, F. J.; Liz-Marzán, L. M. *Langmuir* **2006**, *22*, 7007–7010.

emission spectroscopy (ICP-OES) analysis in a Perkin−Elmer Model Optima 4300-DV ICP-OES spectrometer.

Characterization. UV−vis spectra were recorded using an Agilent Model 8453 UV−vis spectrophotometer. Transmission electron microscopy (TEM) analysis was performed with a JEOL Model JEM 1010 microscope operating at an acceleration voltage of 100 kV. Photon correlation spectroscopy (PCS) was performed on a Zetasizer Nano S (Malvern Instruments, Malvern, U.K.), using a detection angle of 173° and a 4mW He−Ne laser operating at 633 nm. The intensity-averaged particle diameter and the polydispersity index (PDI) values were calculated from cumulant-type analysis.

Kinetic Measurements. The reactions were conducted at different temperatures in quartz cuvettes (thermostatted with an accuracy of 0.2 °C), within a diode-array UV/vis spectrophotometer (Agilent Model 8453). All reaction mixtures were maintained at pH 12, to avoid $NaBH_4$ decomposition.[36] Kinetic data were satisfactorily fitted by first-order integrated rate equations in hexacyanoferrate concentration. Experiments were reproducible to within 5%.